Supplementary Information to Discovery of a wind-driven diamagnetic current system in the Martian magnetosphere

Yuki Harada[1,2*], Robert J. Lillis[3], Matthew O. Fillingim[3], Shun Imajo[4], Takuto Minami[5], Yingjuan Ma[6], Jacob R. Gruesbeck[7], Gina A. DiBraccio[7], Jared R. Espley[7]

[1*]Department of Geophysics, Graduate School of Science, Kyoto University, Kyoto, Japan.
[2*]Institute for Space-Earth Environmental Research, Nagoya University, Nagoya, Japan.
[3]Space Sciences Laboratory, University of California Berkeley, Berkeley, CA, USA.
[4]Data Analysis Center for Geomagnetism and Space Magnetism, Graduate School of Science, Kyoto University, Kyoto, Japan.
[5]Department of Planetology, Graduate School of Science, Kobe University, Kobe, Japan.
[6]Department of Earth Planetary and Space Sciences, UCLA, Los Angeles, CA, USA.
[7]NASA Goddard Space Flight Center, Greenbelt, MD, USA.

*Corresponding author(s). E-mail(s): haraday@kugi.kyoto-u.ac.jp;

1 Supplementary Results

Figures 1a–1c show the local time-latitude distributions of the average magnetic field deviation derived from the MAVEN data at 200-300 km altitudes. We observe characteristic spatial patterns of each component, particularly prominent on the dayside: weak negative (positive) B_r in the northern (southern) hemisphere on the dayside (Figure 1a); negative (positive) B_θ in the dawn to pre-noon sectors and around the noon equator (at post-noon high latitudes and in the dusk sector) (Figure 1b); and

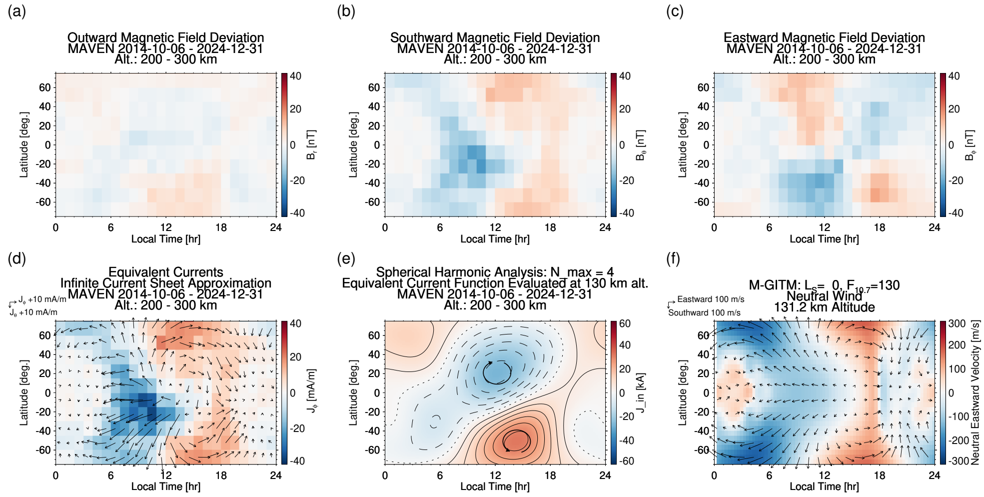

Fig. 1 Average local time-latitude distributions of magnetic fields at 200–300 km altitudes observed by MAVEN and derived equivalent ionospheric currents in comparison to a model neutral wind distribution in the Martian thermosphere. (a–c) Local time-latitude distributions of average magnetic field deviations (derived by subtracting model crustal fields from observed magnetic fields) at 200–300 km altitudes. (d) Equivalent ionospheric currents derived from the horizontal components of magnetic field deviations with infinite current sheet approximation. (e) Equivalent current function of the "internal" terms derived from a spherical harmonic analysis of the three components of magnetic field deviations. (f) Typical neutral wind field at 131.2 km altitude obtained from the M-GITM model [5]. In panel (e), the contours show the equivalent current function evaluated at 130 km altitude.

negative (positive) B_ϕ in the dawn to noon sectors in the southern (northern) hemisphere and in the post-noon to dusk sectors in the northern (southern) hemisphere (Figure 1c). To quickly visualize which pattern of ionospheric currents below the spacecraft can generate the observed magnetic field deviations, we derive equivalent currents from the horizontal components (Figures 1b–1c) with the infinite current sheet approximation (see, e.g., section 3.6 of [1]) as shown in Figure 1d. In Figure 1d, we observe clockwise (counter-clockwise) currents in the northern (southern) hemisphere on the dayside. This pattern is consistent with the neutral wind pattern in the Martian thermosphere (Figure 1f), suggesting contribution from the wind-driven ionospheric dynamo currents [2, 3] as pointed out by [4] from the curl-B results.

We next present the result of the spherical harmonic analysis (SHA) applied to the average distribution of magnetic field deviation shown in Figures 1a–1c. Figure 1e shows the "internal" (ionospheric) equivalent current function derived from SHA of the three components as described in section 4 of the main text. Here, the equivalent current function is the scalar potential associated with the equivalent currents expressed in units of amperes. Equivalent currents flow along the iso-J contours: positive (red) = counter-clockwise currents; negative (blue) = clockwise currents. The contour intervals are 5 kA. Denser contours correspond to stronger current densities. In Figure 1e, the SHA-derived current function smoothly expresses the aforementioned clockwise (counter-clockwise) current pattern in the northern (southern) hemisphere on the dayside. For example, the strong westward currents with dense contours around the noon equator correspond to the observed northward magnetic field deviation (negative B_θ in Figure 1b). The northward (southward) currents in the northern (southern) hemisphere at morning local times represent the eastward (westward) magnetic field deviation in Figure 1c, and the opposite polarities are seen at evening local times. With SHA, we can obtain smooth distributions of the external (magnetospheric) and internal (ionospheric) currents that best explain the observed magnetic field deviations in a least-squares sense. In the following, we analyze SHA-derived equivalent current functions and investigate their dependencies on upstream drivers, seasons, and crustal magnetic fields.

1.1 Dependencies on IMF B_y

We first investigate the effects of the IMF direction. This is one of the most important controlling factors determining the structure of the solar wind-Mars interaction and resulting current systems [4, 7]. Figure 2 shows equivalent ionospheric current distributions for eastward IMF $+B_y$ (a) and westward IMF $-B_y$ (b) conditions. As shown in Figures 2a1 and 2b1, the equivalent current distributions with the infinite current sheet approximation show stronger northward (southward) currents on the dayside for eastward (westward) IMF conditions. This corresponds to currents flowing in the direction of the solar wind electric field (E_{SW}) in the dayside ionosphere driven by the solar wind interaction, which were demonstrated in MSE coordinates by the previous curl-B analyses [4, 7].

The appearance of the $+E_{\mathrm{SW}}$-ward dayside ionospheric currents leads to deformation of the SHA-derived equivalent current functions in Figures 2a2 and 2b2. We further investigate the equivalent current functions by analyzing individual SHA terms as shown in Figures 2a3–2a8 and 2b3–2b8. By comparing the same terms between the eastward and westward IMF conditions, we can find that (a) the h_1^1 term drastically varies with signs flipped (as highlighted by the red and blue arrows in Figures 2a5 and 2b5) and (b) the other terms remain generally similar between the two IMF directions. Based on these observations, we infer that the global ionospheric currents driven by the solar wind interaction are expressed primarily by the h_1^1 term, which represents noon-midnight meridional currents.

From the SHA results, we can also seek a combination of SHA terms that can represent the morphology of the wind-driven ionospheric dynamo currents. Given the expected neutral wind pattern (Figure 1f), we propose that as a simple combination, the sum of g_1^0 and second-degree terms g_2^* and h_2^* can generally express the global pattern of wind-driven ionospheric currents (Figures 2a9 and 2b9). Figures 2a9 and 2b9 show little variation of the current function for different IMF directions, as expected for neutral wind-driven ionospheric currents.

Figure 3 shows magnetospheric current distributions for eastward and westward IMF conditions. Figures 3a1 and 3b1 show local current distributions around 800 km altitudes derived from the curl-B method according to equation (26.2) of [8], while Figures 3a2–3a9 and 3b2–3b9 show the external equivalent current functions in the same format as Figures 2a2–2a9 and 2b2–2b9. A remarkable feature is the dayside counter-clockwise (clockwise) currents in the northern (southern) hemisphere seen in

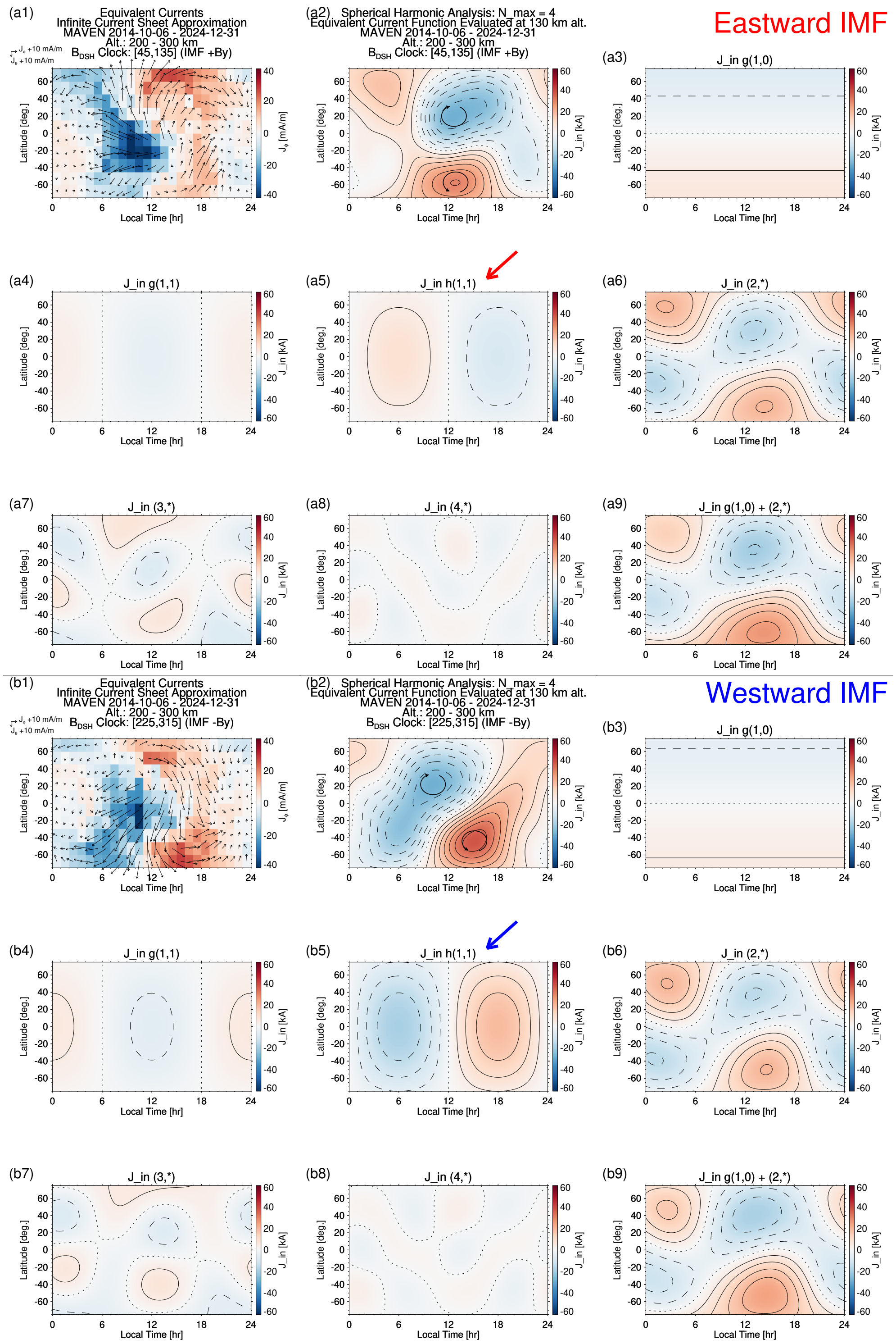

Fig. 2 Equivalent ionospheric current dependence on IMF B_y polarity. Local time-latitude distributions of equivalent currents with infinite current sheet approximation (a1 and b1), SHA-derived equivalent current functions of all internal terms combined (a2 and b2) and contributions from different terms (a3–a9 and b3–b9) are shown for the eastward IMF $+B_y$ (a) and westward IMF $-B_y$ (b) cases.

both curl-B (Figures 3a1 and 3b1) and SHA results (Figures 3a2 and 3b2) regardless of the IMF polarity. This magnetospheric current pattern is opposite to that of the wind-driven ionospheric currents (Figures 1d–1e) and is expressed by the sum of q_1^0 and the second-degree terms q_2^* and s_2^* (highlighted by the pink boxes in Figures 3a9 and 3b9) in a similar manner to the ionospheric case (Figures 2a9 and 2b9).

Meanwhile, the s_1^1 term indicates the southward (northward) magnetospheric currents on the dayside for eastward (westward) IMF conditions as highlighted by the red and blue arrows in Figures 3a5 and 3b5, corresponding to $-E_{\mathrm{SW}}$-ward dayside currents and $+E_{\mathrm{SW}}$-ward nightside currents. This is consistent with the $-E_{\mathrm{SW}}$-ward magnetopause and bow shock currents on the dayside and $+E_{\mathrm{SW}}$-ward currents flowing in the nightside magnetotail as previously identified by [7]. It is worth noting that the presented SHA results are derived from low-altitude (200-300 km) data, yet they successfully identify the contributions from external current sources that were found by the previous local current analyses with the curl-B method.

1.2 Dependencies on Solar Wind Dynamic Pressure

We next investigate dependencies of the ionospheric and magnetospheric currents on the solar wind dynamic pressure, which controls the compression/expansion of the Martian magnetosphere and ionosphere [9, 10]. Figure 4 shows equivalent ionospheric current functions of all terms (top row), the h_1^1 term only (middle row), and $g_1^0+g_2^*+h_2^*$ terms (bottom row) under low (a and c) and high (b and d) dynamic pressure conditions for eastward (a and b) and westard (c and d) IMF directions. The morphology of the total current function varies between low and high dynamic pressure conditions for both eastward (Figures 4a1 and 4b1) and westward (Figures 4c1 and 4d1) IMF polarities. This difference arises mainly from the h_1^1 term enhanced under high dynamic pressure conditions (Figures 4a2–4d2), suggesting that the solar wind interaction-driven ionospheric currents are enhanced by high dynamic pressures. In contrast to the relatively clear trend of the h_1^1 term, the neutral wind-driven ionospheric dynamo currents represented by the $g_1^0 + g_2^* + h_2^*$ terms display little dependence on the solar wind dynamic pressure (Figures 4a3–4d3).

Figure 5 shows equivalent magnetospheric current functions in the same format as Figure 4. We find that these magnetospheric currents vary markedly between the low and high dynamic pressure conditions, particularly in the s_1^1 term, which is enhanced under high dynamic pressure conditions (Figures 4a2–4d2). This suggests that the contributions from the magnetopause, bow shock, and magnetotail currents depend on the solar wind dynamic pressure. The $q_1^0 + q_2^* + s_2^*$ terms show enhanced intensities under high dynamic pressure conditions for the eastward IMF direction (Figures 4a3 and 4b3), but this trend is unclear in the westward IMF direction (Figures 4c3 and 4d3).

1.3 Dependencies on Seasons

We now look at the seasonality of the ionospheric and magnetospheric currents. This is particularly relevant to neutral wind-driven ionospheric currents because seasonal

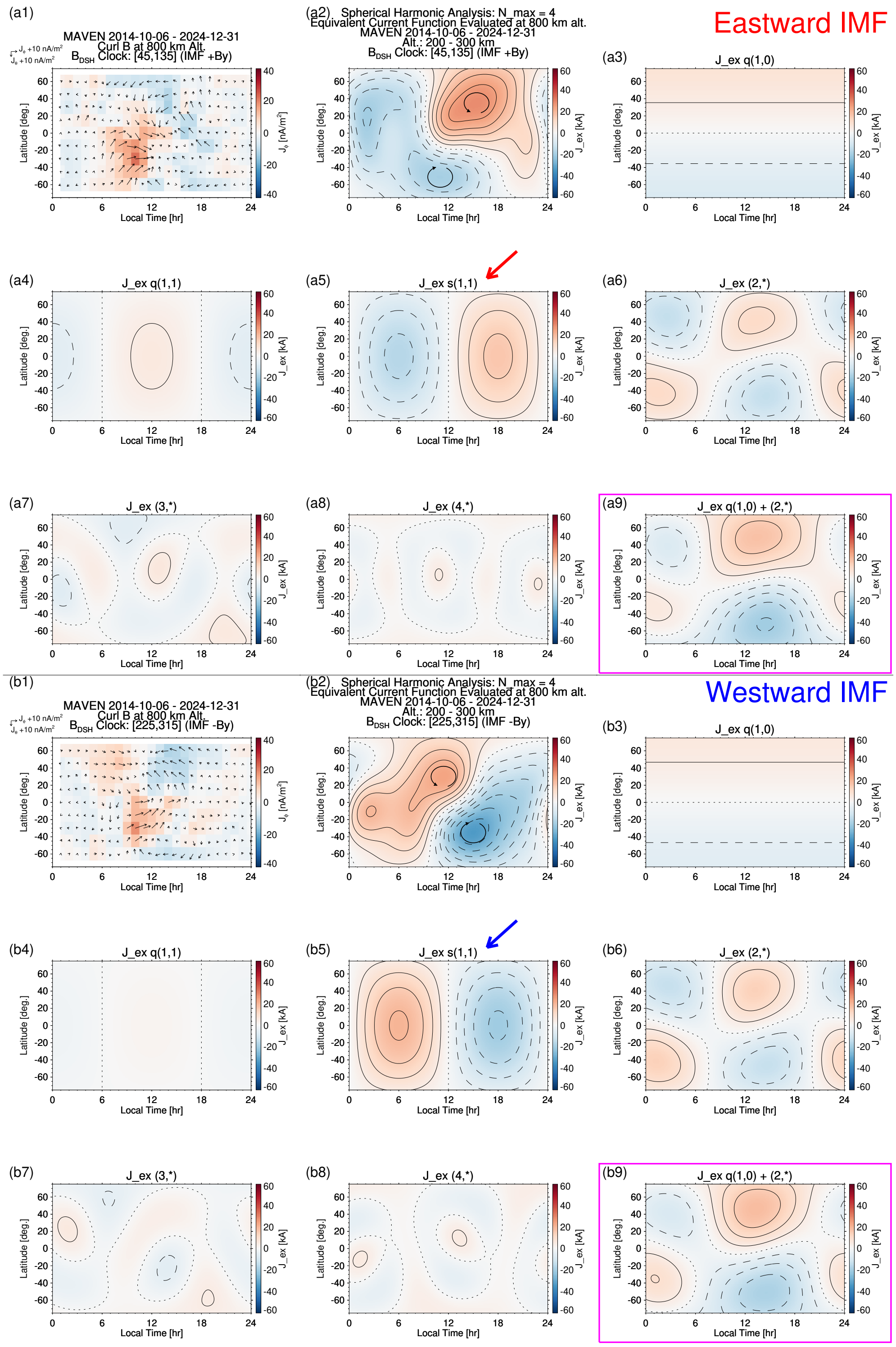

Fig. 3 External magnetospheric current dependence on IMF B_y polarity. Local time-latitude distributions of local current density at 800 km altitude derived from curl-B technique using average magnetic field distributions at 400–800 and 800–1200 km altitudes (a1 and b1), SHA-derived equivalent current functions of all external terms combined (a2 and b2) and contributions from different terms (a3–a9 and b3–b9) are shown for the eastward IMF $+B_y$ (a) and westward IMF $-B_y$ (b) cases.

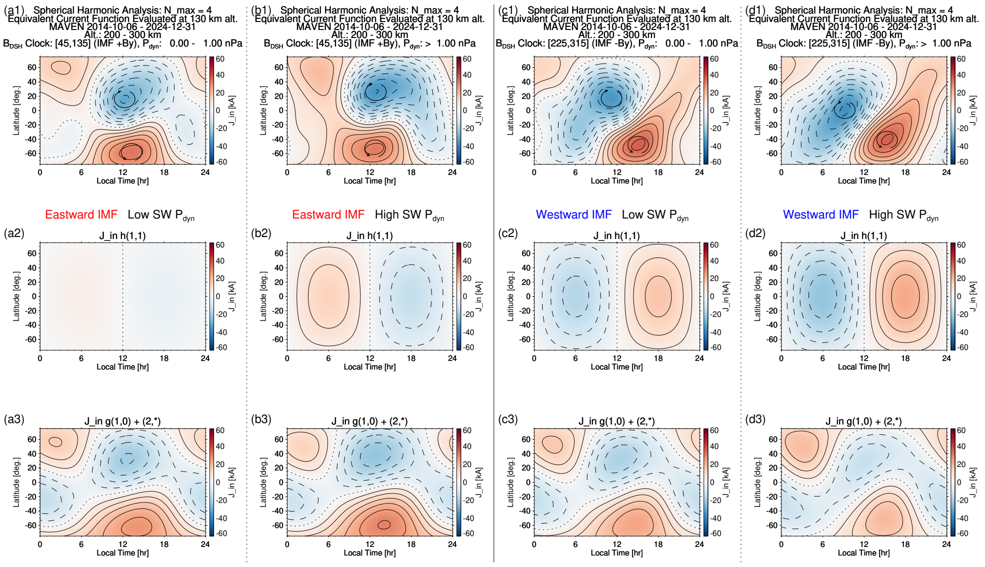

Fig. 4 Equivalent ionospheric current dependence on solar wind dynamic pressure. Local time-latitude distributions of SHA-derived equivalent current functions of all internal terms combined (a1, b1, c1, and d1), the h_1^1 term only (a2, b2, c2, and d2), and $g_1^0 + g_2^* + h_2^*$ terms (a3, b3, c3, and d3) for the eastward IMF $+B_y$ and low dynamic pressure (a), eastward IMF $+B_y$ and high dynamic pressure (b), westward IMF $-B_y$ and low dynamic pressure (c), and westward IMF $-B_y$ and high dynamic pressure (d) conditions.

variations are expected in the neutral wind pattern in the thermosphere. Figure 6 compares equivalent ionospheric currents and model neutral winds for different seasons. It is hard to discern clear global trends of equivalent ionospheric current distributions because of the sampling gaps in the local time-latitude distributions for each season (Figures 6a1–6d1). Nevertheless, we can identify systematic variations in both equivalent ionospheric currents and model neutral winds at evening local times (indicated by the vertical dotted lines in Figures 6a1–6d1 and 6a2–6d2). In Figures 6a3–6d3, we compare the latitude profiles of θ components of the equivalent ionospheric currents derived from the infinite current sheet approximation (black) and SHA (red) with those of the southward component of the neutral wind velocity (blue). We observe that southward (northward) currents prevail around the equator at $L_S \sim 90°$ ($L_S \sim 270°$) just as the neutral winds do (Figures 6b3 and 6d3), suggesting that the ionospheric currents vary seasonally along with thermospheric neutral winds as inferred from ground measurements [11].

Figure 7 illustrates seasonal variations of the equivalent ionospheric current function for eastward (a–d) and westward (e–h) IMF polarities. We observe seasonal variations in the $g_1^0 + g_2^* + h_2^*$ terms, which likely represent seasonally varying wind-driven ionospheric dynamo currents (Figures 7a3–7h3). Seasonal variations are also seen in the h_1^1 term that can be interpreted as ionospheric currents driven by the solar wind interaction (Figures 7a2–7h2). Curiously, we observe small h_1^1 terms at $L_S \sim 180$ and $L_S \sim 270$ for the eastward IMF condition in Figures 7c2 and 7d2, while they

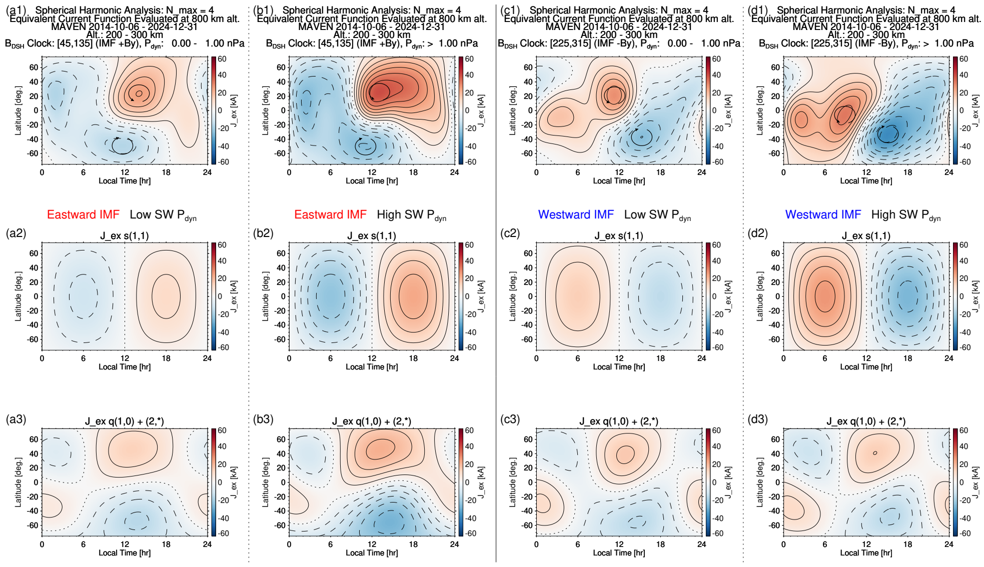

Fig. 5 Equivalent magnetospheric current dependence on solar wind dynamic pressure. Local time-latitude distributions of SHA-derived equivalent current functions of all external terms combined (a1, b1, c1, and d1), the s_1^1 term only (a2, b2, c2, and d2), and $q_1^0 + q_2^* + s_2^*$ terms (a3, b3, c3, and d3) for the eastward IMF $+B_y$ and low dynamic pressure (a), eastward IMF $+B_y$ and high dynamic pressure (b), westward IMF $-B_y$ and low dynamic pressure (c), and westward IMF $-B_y$ and high dynamic pressure (d) conditions.

are well developed for the westward IMF condition in Figures 7g2 and 7h2. Their seasonality may originate from seasonal variations of ionospheric conductivities and heliospheric distance, but specific reasons for the observed variations remain elusive.

Figure 8 shows seasonal variations of the equivalent magnetospheric current function in the same format as Figure 7. The $q_1^0 + q_2^* + s_2^*$ terms (Figures 8a3–8h3) show seasonal variations similar to the equivalent ionospheric currents (Figures 7a3–7h3) except for the opposite signs, suggesting that the two current systems are closely related. Meanwhile, we observe seasonal variations in the s_1^1 term (Figures 8a2–8h2), but their variabilities in the westward IMF condition (Figures 8e2–8h2) are not as distinct as the corresponding ionospheric h_1^1 terms (Figures 7e2–7h2).

1.4 Dependencies on Crustal Magnetic Fields

Finally, we investigate dependencies of ionospheric and magnetospheric currents on crustal magnetic fields of Mars. The Martian crustal fields play a unique role in not only modifying ionospheric properties [12–15] but also shaping the global structure of the Martian magnetosphere [16, 17]. Figure 9 compares equivalent ionospheric current functions in weak ($|B_{\mathrm{c,150km}}| < 20$ nT, where $|B_{\mathrm{c,150km}}|$ is the model crustal field strength at a 150 km altitude for a given geographic longitude and latitude) and moderate and strong ($|B_{\mathrm{c,150km}}| > 20$ nT) crustal field regions for eastward and westward IMF polarities. The $g_1^0 + g_2^* + h_2^*$ terms show clear enhancements in moderate and

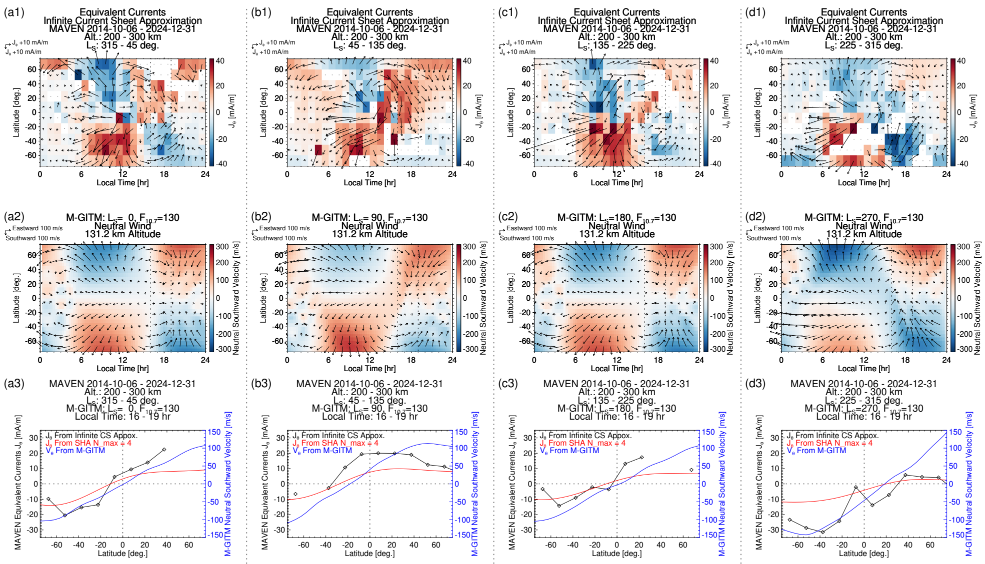

Fig. 6 Seasonal variability of equivalent ionospheric currents and model neutral winds. Local time-latitude distributions of equivalent currents with infinite current sheet approximation (a1, b1, c1, and d1), M-GITM neutral wind distributions (a2, b2, c2, and d2), and latitude profiles of the southward components of the equivalent ionospheric currents with infinite current sheet approximation (black), the equivalent ionospheric currents derived from the spherical harmonic analysis (red), and the M-GITM neutral wind velocity in a local time range of 16–19 hr (a3, b3, c3, and d3) for L_S ranges of 315°–45° (a), 45°–135° (b), 135°–225° (c), and 225°–315° (d).

strong crustal field regions (Figures 9a3–9d3). This suggests that the wind-driven ionospheric dynamo currents are enhanced in moderate and strong crustal field regions. The h_1^1 term displays a seemingly enigmatic behavior. It becomes weaker in strong crustal field regions for the eastward IMF condition (Figures 9a2 and 9b2), while it is only slightly enhanced for the westward IMF condition (Figures 9c2 and 9d2).

Figure 10 shows equivalent magnetospheric current functions in the same format as Figure 9. We observe enhanced $q_1^0 + q_2^* + s_2^*$ terms in moderate and strong crustal field regions (Figures 10a3–10d3) in a similar manner to the $g_1^0 + g_2^* + h_2^*$ terms of the equivalent ionospheric current function (Figures 9a3–9d3). The s_1^1 term, on the other hand, shows a decrease in moderate and strong crustal field regions for the eastward IMF condition (Figures 10a2 and 10b2), while almost no change is observed for the westward IMF condition (Figures 10c2 and 10d2).

Since the results presented so far are derived from local time-latitude distributions averaged over longitudes, an instantaneous global current system at a given moment could significantly differ from the longitude-averaged distributions. Figures 11 and 12 show local time-latitude distributions of equivalent ionospheric and magnetospheric currents, respectively, in narrow subsolar longitude ranges, effectively displaying instantaneous geographic maps as indicated by the gray contours of crustal magnetic field strengths. Since the crustal fields are nonuniformly distributed over

Mars, crustal field effects on the ionospheric and magnetospheric currents vary significantly depending on the subsolar longitude. It can be seen from Figures 11 and 12 that the equivalent ionospheric and magnetospheric currents change their morphology dynamically as Mars rotates (different rows) and when the IMF polarity changes (different columns). The instantaneous ionospheric and magnetospheric current systems can have complicated morphology with significant locality that is highly deformed from the global average distributions characterized by relatively simple spatial patterns.

2 Discussion on Crustal Field Dependence of Wind-Driven Ionospheric Dynamo Currents

Here we discuss the dependence of wind-driven ionospheric dynamo currents on crustal field strengths. In Figures 9a3–9d3, we observe the enhancement of the equivalent ionospheric current function by a factor of a few in strong crustal field regions. [18] investigated the dependence of ionospheric dynamo currents on magnetic field strength using a local multifluid magnetohydrodynamic model that includes collisional effects in the Martian ionosphere. They compared two cases with vertical and uniform magnetic fields of different strengths, but otherwise the same initial conditions. Their results show that stronger ionospheric dynamo currents are produced in the case with the stronger magnetic field because the ionospheric dynamo region is formed at lower altitudes near the electron density peak. This is qualitatively consistent with the results shown in Figures 9a3–9d3. For a quantitative evaluation of the crustal field effects on ionospheric dynamo currents, it is necessary to conduct more in-depth data analyses taking into account the realistic configuration of the Martian crustal magnetic fields, which are beyond the scope of this paper.

Here we conduct a simple test regarding our interpretation of wind-driven ionospheric dynamo currents. As discussed by [2], the wind-driven ionospheric dynamo current can be expressed as follows:

$$\mathbf{J}_{\mathrm{wind}} = B[\sigma_p \mathbf{U} \times \mathbf{b} + \sigma_h \mathbf{U}_\perp], \tag{1}$$

where B is the magnetic field strength, σ_p and σ_h are the Pedersen and Hall conductivities, $\mathbf{U}$ is the neutral wind vector, $\mathbf{b}$ is the magnetic field unit vector, and $\mathbf{U}_\perp$ is the neutral wind perpendicular to the background magnetic field. Let us consider wind-driven ionospheric currents flowing in a radial crustal magnetic field (Figure 13). We can see from equation (1) that the wind-driven Pedersen current depends on the background magnetic field polarity ($\mathbf{b}$) while the wind-driven Hall current does not. This property provides a testable prediction that the total current should rotate counter-clockwise (clockwise) from the cross-field wind direction due to the leftward (rightward) Pedersen current in downward (upward) crustal fields. Figure 14 shows the results of such analysis. Figures 14a and 14b show the equivalent ionospheric currents with the infinite current sheet approximation in radially outward and inward crustal fields, respectively. The overall patterns appear similar, but we can find a small yet systematic difference between the two. Figure 14c compares the current vectors between the outward and inward crustal fields in the same local time-latitude bins. We observe more counter-clockwise rotations from red to blue than clockwise rotations, particularly for strong currents (long arrows). The systematic trend is demonstrated in Figure 14d, which shows histograms of $|\mathbf{J}_{+B_r} - \mathbf{J}_{-B_r}|/|\mathbf{J}_{+B_r} + \mathbf{J}_{-B_r}|$ signed such that the sign of this quantity becomes positive if the rotation is consistent with that expected from Figure 13 (i.e., counter-clockwise rotation from red to blue in Figure 14c), while its magnitude represents the ratio of J_p/J_h. From Figure 14d, we can see that the vast majority of the derived equivalent currents are consistent with the prediction and that the inferred J_p/J_h is below 0.4 as expected from higher Hall conductivity than Pedersen conductivity in the Martian ionospheric dynamo region [2].

References

[1] Yamazaki, Y. & Maute, A. Sq and EEJ—A Review on the Daily Variation of the Geomagnetic Field Caused by Ionospheric Dynamo Currents. *Space Sci. Rev.* **206**, 299–405 (2017). URL https://doi.org/10.1007/s11214-016-0282-z.

[2] Lillis, R. J. *et al.* Modeling wind-driven ionospheric dynamo currents at mars: Expectations for insight magnetic field measurements. *Geophysical Research Letters* **46**, 5083–5091 (2019). URL https://agupubs.onlinelibrary.wiley.com/doi/abs/10.1029/2019GL082536.

[3] Mittelholz, A. *et al.* The origin of observed magnetic variability for a sol on mars from insight. *Journal of Geophysical Research: Planets* **125**, e2020JE006505 (2020). URL https://agupubs.onlinelibrary.wiley.com/doi/abs/10.1029/2020JE006505. E2020JE006505 10.1029/2020JE006505.

[4] Gao, J. *et al.* Two distinct current systems in the ionosphere of mars. *Nature Communications* **15**, 9704 (2024). URL https://doi.org/10.1038/s41467-024-54073-9.

[5] Bougher, S. W. *et al.* Mars Global Ionosphere-Thermosphere Model: Solar cycle, seasonal, and diurnal variations of the Mars upper atmosphere. *J. Geophys. Res.* **120**, 311–342 (2015). URL http://dx.doi.org/10.1002/2014JE004715.

[6] Fournier, A., Aubert, J. & Thébault, E. A candidate secular variation model for igrf-12 based on swarm data and inverse geodynamo modelling. *Earth, Planets and Space* **67**, 81 (2015). URL https://doi.org/10.1186/s40623-015-0245-8.

[7] Ramstad, R. *et al.* The global current systems of the martian induced magnetosphere. *Nature Astronomy* (2020). URL https://doi.org/10.1038/s41550-020-1099-y.

[8] Fillingim, M. *Ionospheric Currents at Mars and Their Electrodynamic Effects*, Ch. 26, 445–458 (American Geophysical Union (AGU), 2018). URL https://agupubs.onlinelibrary.wiley.com/doi/abs/10.1002/9781119324522.ch26. https://agupubs.onlinelibrary.wiley.com/doi/pdf/10.1002/9781119324522.ch26.

[9] Halekas, J. S. *et al.* Structure, dynamics, and seasonal variability of the mars-solar wind interaction: MAVEN solar wind ion analyzer inflight performance and science results. *J. Geophys. Res.* **121**, 547–578 (2016). URL http://dx.doi.org/10.1002/2016JA023167.

[10] Halekas, J. S. *et al.* The day the solar wind disappeared at mars. *Journal of Geophysical Research: Space Physics* **128**, e2023JA031935 (2023). URL https://agupubs.onlinelibrary.wiley.com/doi/abs/10.1029/2023JA031935. E2023JA031935 2023JA031935.

[11] Mittelholz, A. *et al.* Mars' external magnetic field as seen from the surface with insight. *Journal of Geophysical Research: Planets* **128**, e2022JE007616 (2023). URL https://agupubs.onlinelibrary.wiley.com/doi/abs/10.1029/2022JE007616. E2022JE007616 2022JE007616.

[12] Andrews, D. J. *et al.* Control of the topside martian ionosphere by crustal magnetic fields. *Journal of Geophysical Research: Space Physics* **120**, 3042–3058 (2015). URL https://agupubs.onlinelibrary.wiley.com/doi/abs/10.1002/2014JA020703.

[13] Andrews, D. J. *et al.* Electron densities and temperatures in the martian ionosphere: Maven lpw observations of control by crustal fields. *Journal of Geophysical Research: Space Physics* **128**, e2022JA031027 (2023). URL https://agupubs.onlinelibrary.wiley.com/doi/abs/10.1029/2022JA031027. E2022JA031027 2022JA031027.

[14] Flynn, C. L. *et al.* MAVEN Observations of the Effects of Crustal Magnetic Fields on Electron Density and Temperature in the Martian Dayside Ionosphere. *Geophys. Res. Lett.* **44**, 10,812–10,821 (2017). URL http://dx.doi.org/10.1002/2017GL075367.

[15] Sakai, S. *et al.* Low electron temperatures observed at mars by maven on dayside crustal magnetic field lines. *Journal of Geophysical Research: Space Physics* **124**, 7629–7637 (2019). URL https://agupubs.onlinelibrary.wiley.com/doi/abs/10.1029/2019JA026961.

[16] DiBraccio, G. A. *et al.* The Twisted Configuration of the Martian Magnetotail: MAVEN Observations. *Geophys. Res. Lett.* **45** (2018). URL https://agupubs.onlinelibrary.wiley.com/doi/abs/10.1029/2018GL077251.

[17] Xu, S. *et al.* Open magnetic fields in the martian magnetosphere revealing dipole-like intrinsic magnetic fields at mars. *The Astrophysical Journal Letters* **957**, L29 (2023). URL https://dx.doi.org/10.3847/2041-8213/ad0784.

[18] Riousset, J. A. *et al.* Three-dimensional multifluid modeling of atmospheric electrodynamics in Mars' dynamo region. *J. Geophys. Res.* **118**, 3647–3659 (2013). URL http://dx.doi.org/10.1002/jgra.50328.

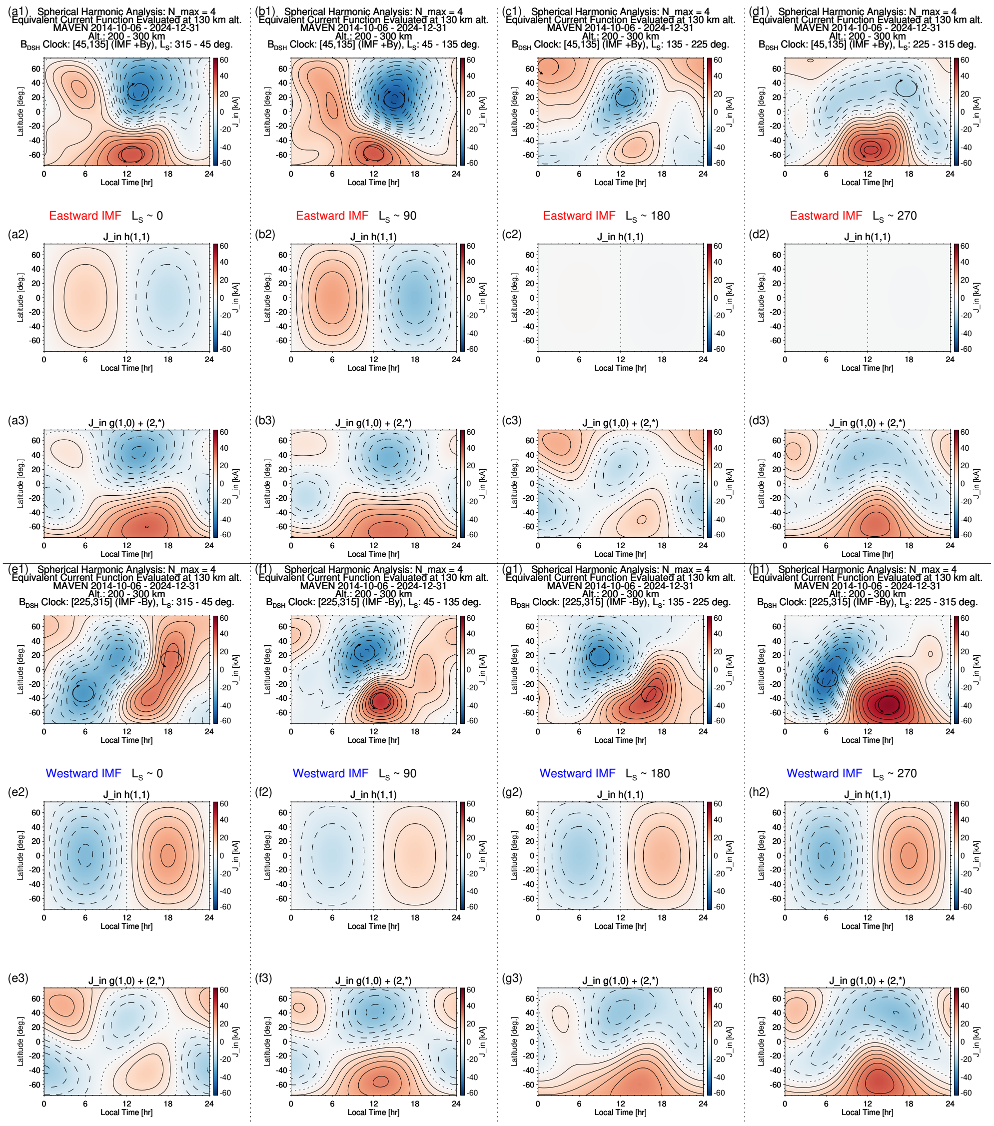

Fig. 7 Seasonal variability of equivalent ionospheric currents. Local time-latitude distributions of SHA-derived equivalent current functions of all internal terms combined (a1, b1, c1, d1, e1, f1, g1, and h1), the h_1^1 term only (a2, b2, c2, d2, e2, f2, g2, and h2), and $g_1^0 + g_2^* + h_2^*$ terms (a3, b3, c3, d3, e3, f3, g3, and h3) for L_S ranges of 315°–45° (a and e), 45°–135° (b and f), 135°–225° (c and g), and 225°–315° (d and h) for the eastward IMF $+B_y$ (a–d) and westward IMF $-B_y$ (e–h) conditions.

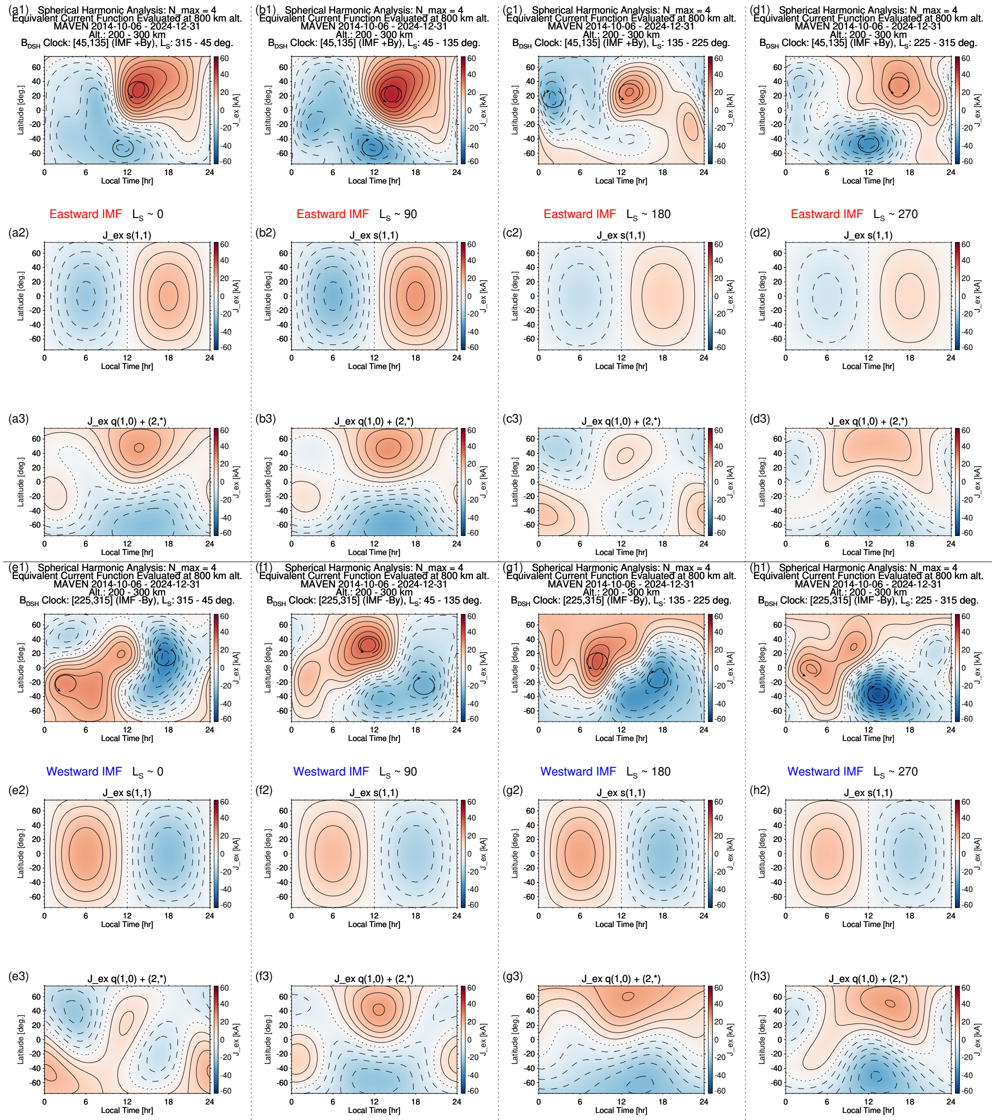

Fig. 8 Seasonal variability of equivalent magnetospheric currents. Local time-latitude distributions of SHA-derived equivalent current functions of all external terms combined (a1, b1, c1, d1, e1, f1, g1, and h1), the s_1^1 term only (a2, b2, c2, d2, e2, f2, g2, and h2), and $q_1^0 + q_2^* + s_2^*$ terms (a3, b3, c3, d3, e3, f3, g3, and h3) for L_S ranges of 315°–45° (a and e), 45°–135° (b and f), 135°–225° (c and g), and 225°–315° (d and h) for the eastward IMF $+B_y$ (a–d) and westward IMF $-B_y$ (e–h) conditions.

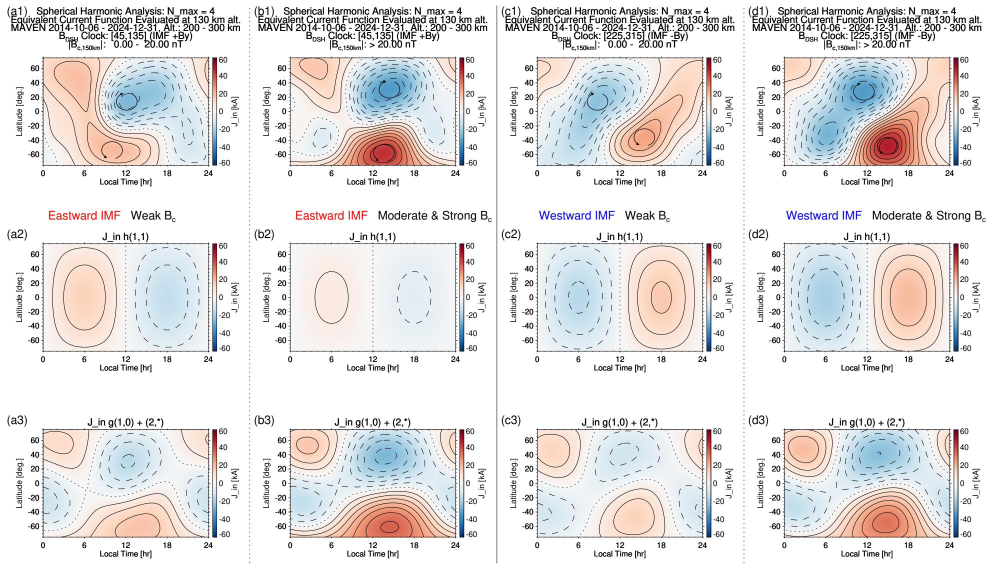

Fig. 9 Equivalent ionospheric current dependence on crustal field strength. Local time-latitude distributions of SHA-derived equivalent current functions of all internal terms combined (a1, b1, c1, and d1), the h_1^1 term only (a2, b2, c2, and d2), and $g_1^0 + g_2^* + h_2^*$ terms (a3, b3, c3, and d3) in weak (a and c) and moderate and strong (b and d) crustal field regions for the eastward IMF $+B_y$ (a and b) and westward IMF $-B_y$ (c and d) cases.

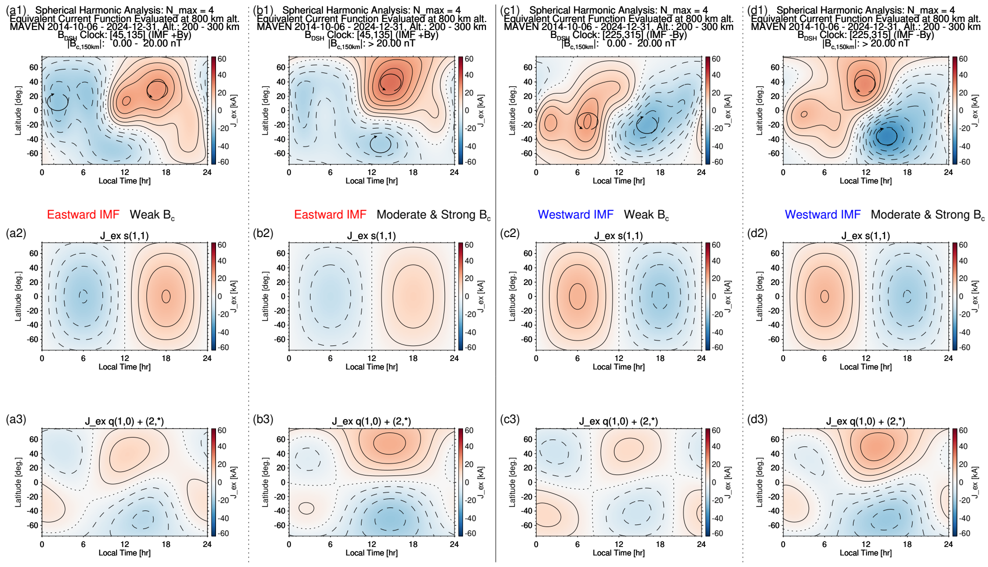

Fig. 10 Equivalent magnetospheric current dependence on crustal field strength. Local time-latitude distributions of SHA-derived equivalent current functions of all external terms combined (a1, b1, c1, and d1), the s_1^1 term only (a2, b2, c2, and d2), and $q_1^0 + q_2^* + s_2^*$ terms (a3, b3, c3, and d3) in weak (a and c) and moderate and strong (b and d) crustal field regions for the eastward IMF $+B_y$ (a and b) and westward IMF $-B_y$ (c and d) cases.

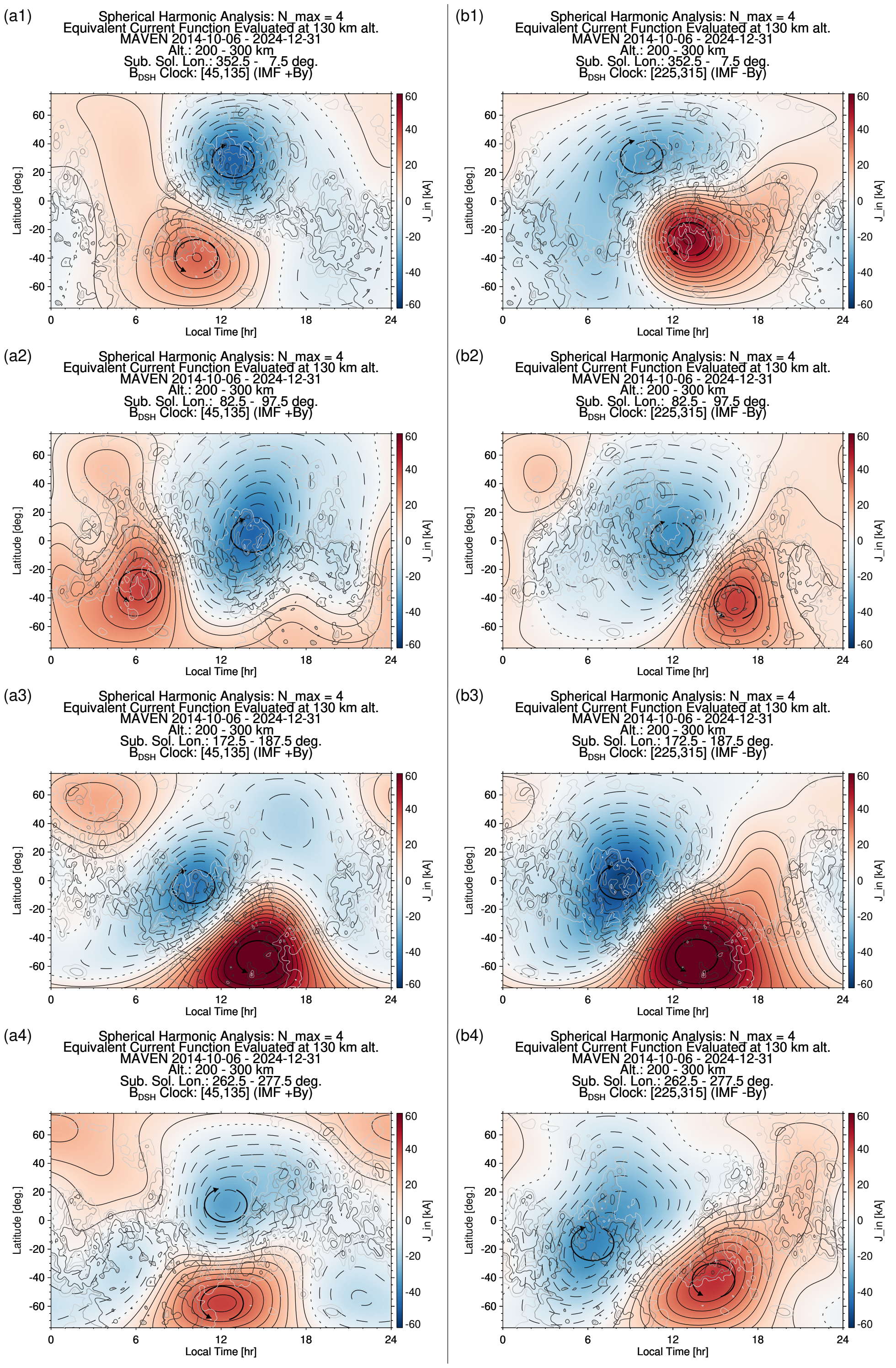

Fig. 11 Equivalent ionospheric current dependence on subsolar longitude. Local time-latitude distributions of SHA-derived internal equivalent current functions for different subsolar longitudes of $\sim 0°$ (a1 and b1), $\sim 90°$ (a2 and b2), $\sim 180°$ (a3 and b3), and $\sim 270°$ (a4 and b4), for eastward IMF $+B_y$ (a) and westward IMF $-B_y$ (b) conditions. The gray contours show the crustal magnetic field distributions ($|B_c| = 20$, 50, and 100 nT at 150 km altitude).

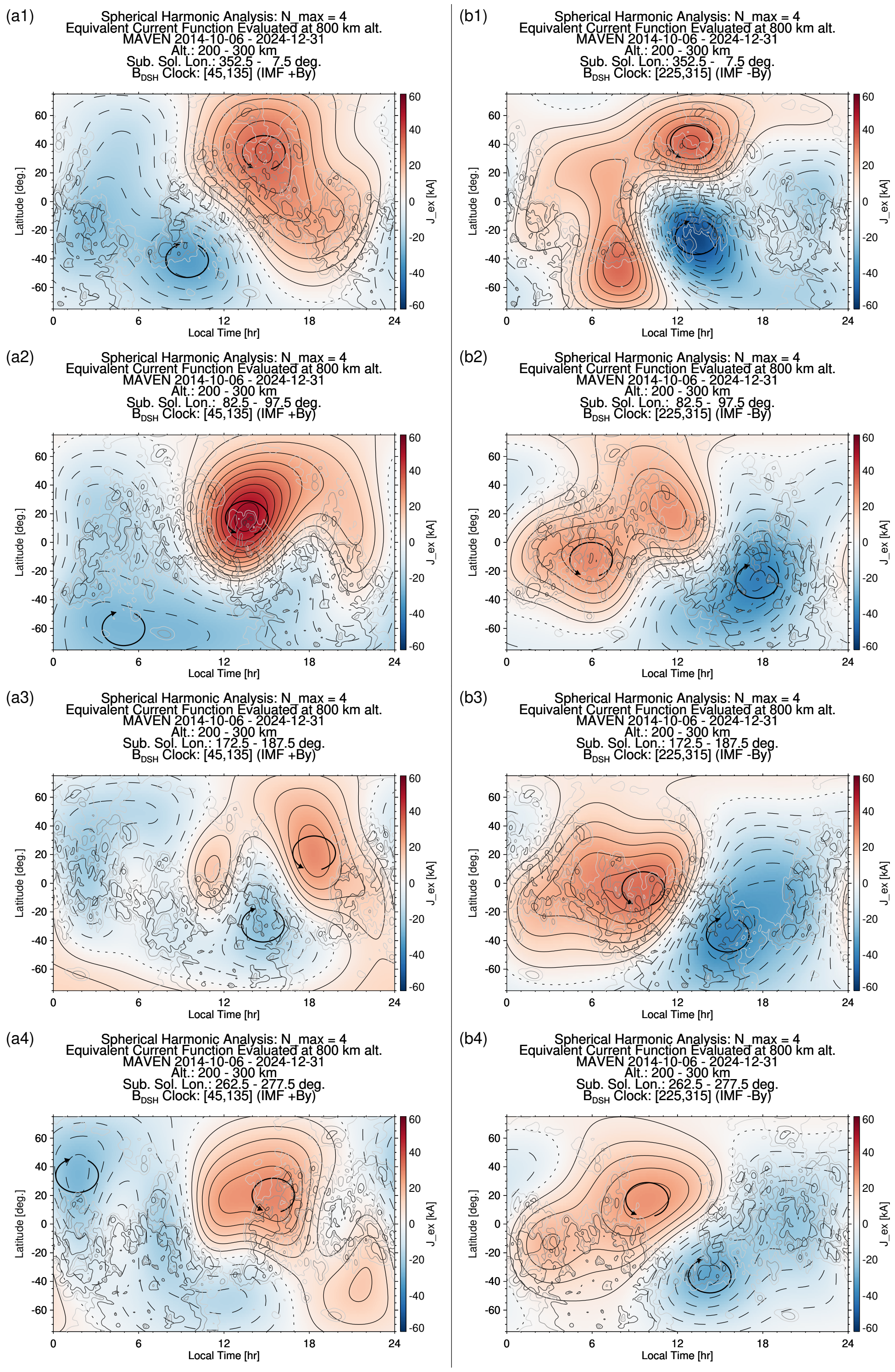

Fig. 12 Equivalent magnetospheric current dependence on subsolar longitude. Local time-latitude distributions of SHA-derived external equivalent current functions for different subsolar longitudes of ∼0° (a1 and b1), ∼90° (a2 and b2), ∼180° (a3 and b3), and ∼270° (a4 and b4), for eastward IMF $+B_y$ (a) and westward IMF $-B_y$ (b) conditions. The gray contours show the crustal magnetic field distributions ($|B_c|$ = 20, 50, and 100 nT at 150 km altitude).

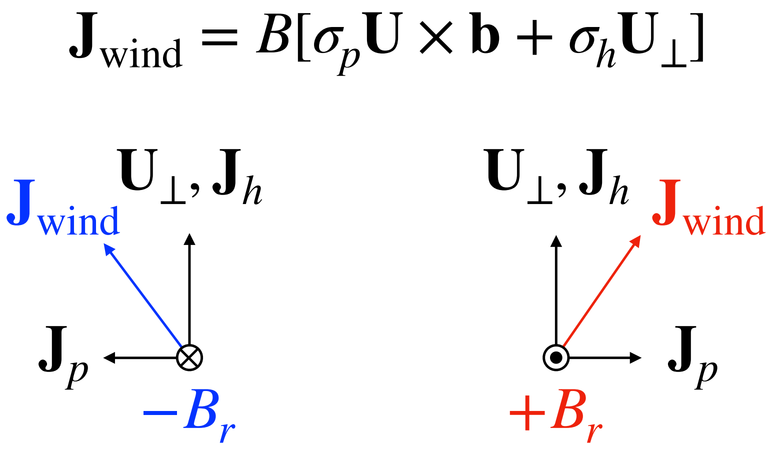

Fig. 13 Schematic illustration of the expected dependence of wind-driven ionospheric currents on the radial component of magnetic fields.

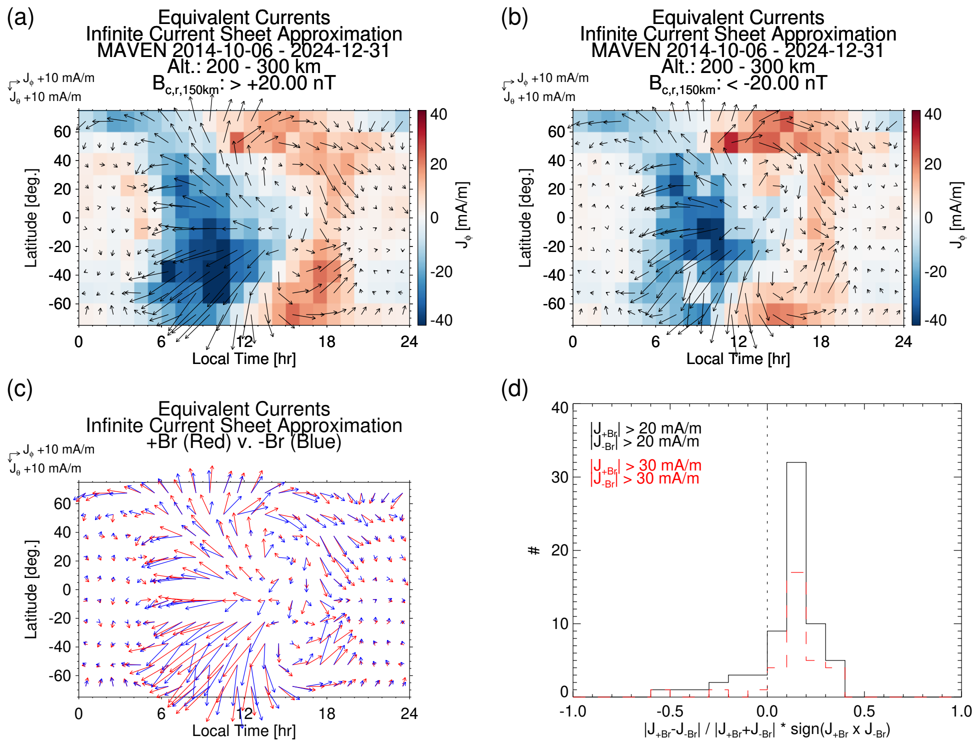

Fig. 14 Equivalent ionospheric current dependence on the radial crustal field component. Local time-latitude distributions of equivalent currents with infinite current sheet approximation for the crustal field radial component of $B_r > +20$ nT ($\mathbf{J}_{+B_r}$, (a)) and $B_r < -20$ nT ($\mathbf{J}_{-B_r}$, (b)). (c) Over-plot of the $\mathbf{J}_{+B_r}$ and $\mathbf{J}_{-B_r}$ vectors. (d) Histograms of $|\mathbf{J}_{+B_r} - \mathbf{J}_{-B_r}|/|\mathbf{J}_{+B_r} + \mathbf{J}_{-B_r}| * \text{sign}(\mathbf{J}_{+B_r} \times \mathbf{J}_{-B_r})$ for relatively strong current vectors (>20 mA/m in black, >30 mA/m in red).